SARS-CoV-2 transmission via apical syncytia release from primary bronchial epithelia and infectivity restriction in children epithelia — Source link ↗

Guillaume Beucher, Marie-Lise Blondot, A. Celle, Noémie Pied ...+16 more authors

Institutions: Centre national de la recherche scientifique, French Institute of Health and Medical Research, University of Bordeaux, University of Regensburg

Related papers:

- Pediatric nasal epithelial cells are less permissive to SARS-CoV-2 replication compared to adult cells

- Expression of SARS-CoV-2 entry factors in lung epithelial stem cells and its potential implications for COVID-19.

- SARS-CoV-2 Infection of Airway Epithelial Cells

- Severe Acute Respiratory Syndrome Coronavirus Infection of Human Ciliated Airway Epithelia: Role of Ciliated Cells in Viral Spread in the Conducting Airways of the Lungs

- Tracking Changes in SARS-CoV-2 Spike: Evidence that D614G Increases Infectivity of the COVID-19 Virus.

1

SARS-CoV-2 transmission via apical syncytia release from primary bronchial epithelia and infectivity restriction in children epithelia

4

Guillaume Beucher[a*], Marie-Lise Blondot[a*], Alexis Celle [b*], Noémie Pied[a,], Patricia Recordon-Pinson[a], Pauline Esteves[b], Muriel Faure[a,], Mathieu Métifiot[a], Sabrina Lacomme[c], Denis Dacheaux[a,], Derrick Robinson[a,], Gernot Längst[d], Fabien Beaufils [b,e], Marie-Edith Lafon[a,f] Patrick Berger[b], Marc Landry[c], Denis Malvy[g], Thomas Trian[b#,] Marie-Line Andreola[a#] and Harald Wodrich[a,#,$]

[a]Univ. Bordeaux, CNRS, Microbiologie Fondamentale et Pathogénicité, UMR 5234, F-33000 Bordeaux, France.
[b]INSERM, Centre de Recherche Cardio-thoracique de Bordeaux, U1045, CIC 1401, Bordeaux, 33000, France.,
[c] University of Bordeaux, CNRS, Institute of Neurodegenerative Diseases, IINS, UMR 5293, Bordeaux, France, University of Bordeaux, CNRS, INSERM, Bordeaux Imaging Center, BIC, UMS 3420, US 4, Bordeaux, France
[d]Biochemistry Center Regensburg, Universität Regensburg, Regensburg, Germany
[e]CHU de Bordeaux, Service d'exploration fonctionnelle respiratoire, service de pédiatrie médicale, CIC 1401, 33000, Bordeaux, France,
[f] CHU de Bordeaux, Laboratoire de Virologie, 33000 Bordeaux, France
[g] Department for infectious and tropical d'idéales, University Hospital center Pellegrin, Bordeaux, & Inserm 1219, University of Bordeaux, Bordeaux, France.

22

Author Contributions: *These authors contributed equally, #These authors contributed equally

Competing Interest Statement: The authors have no competing interest

Keywords: SARS-CoV-2, human bronchial epithelia, Age, Syncytia formation, IFN response

This PDF file includes:

Main Text
Figures 1 to 5
Tables 1
Supplemental Figures S1 to S3

31

Abstract

The beta-coronavirus SARS-CoV-2 is at the origin of a persistent worldwide pandemic. SARS-CoV-2 infections initiate in the bronchi of the upper respiratory tract and are able to disseminate to the lower respiratory tract eventually causing acute severe respiratory syndrome with a high degree of mortality in the elderly. Here we use reconstituted primary bronchial epithelia from adult and children donors to follow the infection dynamic following infection with SARS-CoV-2. We show that in bronchial epithelia derived from adult donors, infections initiate in multi-ciliated cells. Then, infection rapidly spread within 24-48h throughout the whole epithelia. Within 3-4 days, large apical syncytia form between multi-ciliated cells and basal cells, which dissipate into the apical lumen. We show that these syncytia are a significant source of the released infectious dose. In stark contrast to these findings, bronchial epithelia reconstituted from children donors are intrinsically more resistant to virus infection and show active restriction of virus spread. This restriction is paired with accelerated release of IFN compared to adult donors. Taken together our findings reveal apical syncytia formation as an underappreciated source of infectious virus for either local dissemination or release into the environment. Furthermore, we provide direct evidence that children bronchial epithelia are more resistant to infection with SARS-CoV-2 providing experimental support for epidemiological observations that SARS-CoV-2 cases' fatality is linked to age.

Significance Statement

Bronchial epithelia are the primary target for SARS-CoV-2 infections. Our work uses reconstituted bronchial epithelia from adults and children. We show that infection of adult epithelia with SARS-CoV-2 is rapid and results in the synchronized release of large clusters of infected cells and syncytia into the apical lumen contributing to the released infectious virus dose. Infection of children derived bronchial epithelia revealed an intrinsic resistance to infection and virus spread, probably as a result of a faster onset of interferon secretion. Thus, our data provide direct evidence for the epidemiological observation that children are less susceptible to SARS-CoV-2.

Main Text

Introduction

Coronaviruses with zoonotic origin have emerged as a new public health concern during the first decades of the 21th century. Two highly pathogenic coronaviruses, severe acute respiratory

2

65 syndrome coronavirus (SARS-CoV) and Middle-East respiratory syndrome coronavirus (MERS-

66 CoV), caused severe respiratory infections in humans during regionally confined epidemics in

67 2002 (1) and between 2010-15 (2), respectively. In late 2019, clusters of patients with pneumonia

68 in Wuhan in the Hubei province in China were shown to be infected with the novel severe acute

69 respiratory syndrome coronavirus 2 (SARS-CoV-2) (3-5). SARS-CoV-2 infections are associated

70 with acute respiratory illness referred to as Coronavirus disease (COVID-19). Since its description,

71 SARS-CoV-2 infections are at the root of an enduring worldwide pandemic, having caused as of

72 May 2021 over 3 million deaths and more than 148 million confirmed infections (data from the

73 John Hopkins university coronavirus resource center, https://coronavirus.jhu.edu/). SARS-CoV-2

74 is an enveloped virus with a positive single-stranded RNA of around 30 kb. The 5' proximal two

75 thirds of the polyadenylated genome encodes ORF1a and ORF1b, which are autoproteolytically

76 processed into several non-structural proteins required for replication and transcription. The

77 distal third encodes for the 4 structural proteins, Envelope (E), Membrane (M), Nucleocapsid (N)

78 and Spike (S) and seven putative ORFs encoding accessory proteins and potential virulence factors

79 (6-8). The surface exposed Spike protein gives the virus its crown-like appearance in electron

80 microscopy and mediates the attachment to the main cellular receptor ACE2 (9). Coronaviruses

81 can cause a wide range of respiratory illnesses, from mild upper respiratory tract infection up to

82 a severe acute respiratory syndrome (10). The latter is characterized by excessive cytological

83 damage and inflammation. Post mortem biopsies in patients that died from COVID-19 point to

84 airways and lungs as primary targets of the disease (11, 12) with advanced diffuse alveolar

85 damage, pulmonary thrombosis and abnormal syncytia formation (13, 14). Several studies suggest

86 that cytokine storm and inflammatory infiltrates in the alveolar space are associated with disease

87 severity and death in COVID-19 (15, 16). While SARS-CoV-2 is genetically close to SARS-CoV, it

88 shows much higher effective transmissibility (17, 18). One reason for this higher contagiousness

89 is an active virus replication in tissues of the upper respiratory tract at an early stage of infection,

90 with a high number of virus copies produced four days after the beginning of symptoms, and an

91 active replication in the throat (19) (20). Furthermore, Zou et al (21) reported that the viral load

92 detected in asymptomatic patients was similar to that of symptomatic patients on day 4 after

93 symptoms onset, suggesting equal transmission potential of asymptomatic or minimally

94 symptomatic patients at very early stages of infection (22). Epidemiological data have

95 demonstrated that if all ages of the population are susceptible to SARS-CoV-2 infection, SARS-

3

96 CoV-2 infection severity is different between children *versus* the adult populations and varies with

97 age (23). A recent multi-national epidemiologic study found that children under 9 years old have

98 very low case-fatality rates of SARS-CoV-2 infection compared to older patients (24). Moreover,

99 these studies consolidate a large discrepancy in death rates of SARS-CoV-2 infected patients

100 associated with age. Death rate in children (<9 years) is under 0.001% increasing to 8% in elderly

101 patients (>80 years). A recent metadata analysis of several studies came to the same correlation

102 between age and severity (25). The reason for this age-related discrepancy is not clear and could

103 be linked to a decreased transmission and/or viral load with SARS-CoV-2 in children compared to

104 adults. Only limited data are available about the mechanism of viral spreading over time and how

105 the virus is released from the epithelia and might participate in the transmission of the infection

106 between individuals or within an individual. Over the course of a 51 days period, infection of a

107 reconstituted human airway epithelium infected with SARS-CoV-2 showed multiple waves of viral

108 replication associated with a degradation of tight junction and a decrease in ciliary expression (26,

109 27). In this model, plaque-like cytopathic effects could be observed with the formation of multi-

110 nucleated cells (28). Regarding the inflammatory response, interferon induction appears limited

111 in the most severe clinical cases (29-31). In contrast, release of INF-λ was induced at day 4 post-

112 infection of bronchial epithelia (BE). Noteworthy, viral RNA production in BE increased at day 2,

113 suggesting a delay in the induction of the cellular antiviral response. A very recent report studying

114 cell-intrinsic changes occurring in differentiated human nasal epithelial cultures from children,

115 adults and elderly, have shown that ageing contributed to viral load, transcriptional responses,

116 IFN signaling and antiviral responses (32). Yet, such data using a model mimicking the human

117 bronchial epithelium are still missing. Here, we developed a model of reconstituted bronchial

118 epithelium (BE) in air-liquid interface derived from bronchial epithelium samples of adult donors,

119 which is the primary site of SARS-CoV-2 infection. We monitored the replication of SARS-CoV-2

120 over several days and followed virus spread in the epithelia. Using high-resolution imaging, we

121 observed the massive formation and apical release of syncytia occurring between day three and

122 four post-infection. We showed that syncytia and cells released into the apical lumen are

123 infectious, suggesting they contribute to the spreading of the virus in the epithelium, and by

124 extension, may transmit virus within the patient to the lower respiratory tract or into the

125 environment. Furthermore, using reconstituted BE derived from children, we showed that viral

126 production in children epithelia is very low compared to adults, and that viral spread is restricted.

4

127   These results may explain the clinical and epidemiological observations that SARS-CoV-2 is more

128   likely to infect older patients than children and that older patients show more severe clinical

129   manifestations.

130

131   **Results**

132

133   **Generation of a fully differentiated bronchial epithelia model**

134   One of the major initial targets for SARS-CoV-2 is the respiratory tract. Primary infections often

135   initiate in the upper respiratory tract from which they can spread to the lower respiratory tract to

136   cause severe disease (18). Bronchial epithelia are pseudo-stratified cell layers with typical cell

137   junctions, as well as a mucus layer and beating cilia on the lumen side (33, 34). To study the SARS-

138   CoV-2 infection process in a physiologically relevant model, we established a cellular *in vitro*

139   model of bronchial epithelia differentiated in air-liquid interface from individual donors (Fig. S1).

140   Primary bronchial epithelial cells were collected from surgical bronchial resection or fibroscopy

141   from individual adult donors at the Bordeaux university hospital. Patients were between 46 and

142   63 years old with a normal body mass index [BMI] (Table1). Basal epithelial cells were expanded

143   *in vitro* in culture flask until confluence. Basal cells were then seeded on cell culture insert and

144   differentiated at the air-liquid interface for approximately 21 days (Fig. S1A). Using this

145   differentiation protocol, we were able to generate between 12-24 individual inserts from a single

146   donor allowing comparative analysis. Immuno-fluorescence (IF) analysis confirmed the presence

147   of differentiated cell types. Specific antibodies allowed the detection of acetylated tubulin and

148   mucin, characteristic of multi-ciliated cells and goblet cells respectively (Fig. S1B, movie S1) or

149   acetylated tubulin and cytokeratin 5 (multi-ciliated cells and basal cells, Fig. S1C, movie S2). This

150   analysis confirmed the pseudostratified apical-to-basolateral organizational integrity of the

151   epithelia, *e.g.* a single cell layer of apical multi-ciliated cells covering a layer of basal cells and was

152   further confirmed by electron microscopy (Fig. S1D). The presence of well differentiated cilia

153   structures and tight junctions was also confirmed (Fig. S1D). Next, we determined the localization

154   of ACE2, the primary receptor for SARS-CoV-2 in our model using IF analysis (Fig. S1E, movie S3).

155   Co-label with antibodies against ACE2 and acetylated tubulin confirmed that ACE2 was expressed

156   in apical multi-ciliated cells as previously reported (4, 35). Moreover, our data showed a

5

157 prominent exposure of ACE2 on individual cilia reaching into the apical lumen (orange arrows),

158 which suggests facilitated access *e.g.* for virus coming in through the respiratory tract.

159

160 **SARS-CoV-2 monitoring and BE infection**

161 Next, BE were inoculated on the apical side with a suspension of a reference SARS-CoV-2 strain

162 (BetaCoV/France/IDF0372/2020) at a multiplicity of infection (MOI) of 0.012. Apical and

163 basolateral compartments were collected 3 days post-infection (dpi) and used to infect Vero E6

164 cells (Fig. 1A). A cytopathic effect (CPE) was observed in the Vero E6 cell culture as early as 2 days

165 post-infection when inoculated with the apical washes, indicating an effective infection and

166 replication of the virus (Fig. 1A). When using the basal medium, 3 days of inoculation were

167 necessary to observe a similar CPE (Fig. 1A). This faster appearance of CPE when using the apical

168 fraction may be correlated to a higher viral titre compared to the basal medium. To ascertain that

169 this CPE is indeed due to viral replication and not a toxic effect from the inoculation, we extracted

170 total RNAs from the Vero E6 supernatant on the next day (4 dpi) and quantified viral RNAs using

171 in-house qRT-PCR targeting the N-gene region. No RNA could be detected in the supernatant of

172 Vero E6 cells inoculated with either the apical or basolateral fractions obtained from non-infected

173 BE (Fig. 1B, control). In contrast, when using basolateral or the apical fraction from infected BEs,

174 the Vero E6 supernatant contained high level of SARS-CoV-2 RNA, comparable to what is observed

175 with a direct infection of Vero E6 cells infected at a MOI of 0.01 (Fig. 1B). These data attest that

176 SARS-CoV-2 actively replicates in reconstituted BE and that inoculation from the apical side results

177 in an active infection. To detect virus-infected cells, we generated monoclonal antibodies against

178 the SARS-CoV-2 N nucleocapsid protein using bacterially expressed and purified full-length

179 protein as detailed in the methods section. Hybridoma supernatants were tested using western

180 blot and IF detection through confocal microscopy (Fig. S2). Of several positive clones, hybridoma

181 clone 3G9 was selected for this study as it specifically recognized the N protein of SARS-CoV-2

182 (Fig. S2A) and detected infected cells in IF staining (Fig. S2B). To investigate which cell type is the

183 primary target during SARS-CoV-2 infection, fully differentiated epithelia were infected with SARS-

184 CoV-2 at a MOI of 0.01 for 1 h from the apical side after which the viral suspension was removed.

185 Epithelia were fixed 24h post-infection in 4% paraformaldehyde (PFA) and processed for IF

186   analysis using SARS-CoV-2-N specific antibodies. We successfully detected infected cells in the BE

187   (green signal Fig. 1C-E). Specific co-label of Muc5A showed that goblet cells were not infected

188   (magenta signal, Fig. 1C, movie S4). Similarly, no co-localization could be observed between the

189   SARS-CoV-2 N protein and CytK5 showing that basal cells were not infected either (Fig. 1D, movie

190   S5). Conversely, the signal arising for the N protein staining was systematically associated with

191   strong labelling for acetylated tubulin, a specific marker for multi-ciliated cells (orange arrow, Fig.

192   1E, movie S6). This is consistent with previous reports that apical multi-ciliated cells are the

193   primary target cells for SARS-CoV-2 infection (4, 28, 36). In addition, all BEs were co-labelled with

194   fluorescent phalloidin to mark cell boundaries for 3D imaging of the entire epithelial depth.

195   Infected cells were exclusively located at the apical surface of the BE (Fig. 1C-E). All IF data were

196   confirmed using BE generated from at least two different donors, suggesting that the primary

197   infection of epithelial cells is determined by the epithelia architecture and is not due to the genetic

198   background of the donor.

199

Infection kinetic of epithelia from different adult donors

201   To better understand how SARS-CoV-2 spreads in the epithelium after initial infection of multi-

202   ciliated cells, we infected BEs from four individual adult donors (A1 to A4, Table 1) and monitored

203   them over the course of 7 days. Low magnification images obtained using IF microscopy showed

204   that N protein could be detected within 24h of infection in a small number of cells (Fig. 2A).

205   Nonetheless, the signal number and intensity increased drastically from the 2 dpi time-point and

206   tended to decrease slightly towards the end of the observation period (Fig. 2A). Similar results

207   were obtained with the other two donors suggesting rapid onset of viral replication and spread

208   (not shown). We quantified the number of N-positive signals at low resolution for each donor

209   confirming that the number of infected cells strongly increased within two to three days of the

210   initial infection, reaching a maximum around day four, and consistently decreased somewhat on

211   the seventh day for all donors (Fig. 2B). Of note, much larger N protein associated signals could

212   be observed at the peak of the infection. These larger structures were co-labelled with cytokeratin

213   5, the marker for basal cells (see arrows in Fig. 2A). This observation started on the third day but

214   was most prominent on the fourth day and was observed for all donors. Therefore, we also

215   quantified the size of the N protein associated signals over time (Fig. 2C). The analysis revealed a

216   statistically significant average increase in signal size between the third and fourth day for all four

217   donors. In parallel to the imaging analysis, release of newly produced viruses into the apical mucus

218   was quantified by qRT-PCR (Fig. 2D). For all four donors, the viral RNA copy number correlated

219   with the observed cellular N protein labelling with a fast increase from day 2 reaching a plateau

220   between 3 and 4 dpi. Altogether, these data suggested that apical SARS-CoV-2 inoculation of BEs

221   resulted in efficient infection and subsequent progeny production and release into the apical

222   lumen.

223

224   **Infected multi-ciliated cells form syncytia with basal cells at the apical side of the BE**

225   Using high-resolution microscopy, we observed that larger N-positive signals corresponded to

226   multinucleated cellular structures reminiscent of syncytia. These syncytia could be found in all

227   regions of the epithelia (Fig. 3) and their formation at day 4 was common to all four donors tested.

228   In contrast, we did not observe any syncytia formation in non-infected control epithelia.

229   Unexpectedly, the N-positive syncytia forming on day three and four also stained positive for the

230   basal cell marker cytokeratin 5 (Fig. 3A). This was not the case at earlier time points (day one and

231   two) where basal cells rarely stained positive for N protein and did not form syncytia. Accordingly,

232   we quantified the number of double positive syncytia (*i.e,* nucleocapsid protein and cytokeratin

233   5) over time (Fig. 3B). The proportion of double positive cells (*i.e,* syncytia) increased constantly

234   and reached a maximum on the fourth day after which there is a drastic drop in double positive

235   cells (Fig. 3B, upper panel). Normalization of the double positive cells for either the total amount

236   of basal cells (Fig. 3B, middle panel) or the total amount of infected cells (Fig. 3B, lower panel)

237   revealed that double positive cells but not overall infected cells disappeared on day four. We also

238   observed that the newly formed multinucleated cells only partially stained for acetylated tubulin

239   (Fig. 3C). Zooming in on different regions of the epithelia revealed that newly formed syncytia

240   frequently lost their stain for acetylated tubulin (Fig. 3C side panel). Moreover, syncytia that still

241   expressed acetylated tubulin presented an amorphous staining, and rarely distinguished cilia

242   features. Similarly, part of the syncytial structures failed to stain with phalloidin (*e.g.* Fig. 3A, right

243   panel), that was used to delineate cells in the epithelia. Altogether, Cytokeratin 5, phalloidin and

244   acetylated tubulin staining patterns suggested that syncytia were formed through the fusion of

245   infected ciliated cells with basal cells, associated with the loss of cilia and reorganization of

246   cytoskeletal features including the actin and tubulin cytoskeleton. Furthermore, three-

247   dimensional imaging of epithelia showed that syncytia formed exclusively on the apical side of the

248   epithelium and forming an elevated layer on top of the epithelia (Fig. 3A right and 3C bottom

249   panel, see also movie S7 and S8). These extrusions were also observed using EM (Fig. 3D, white

250   asterisk), but never in the context of non-infected epithelia (Fig. S1). These structures harbored

251   only reminiscent cilia structures in place of multi-ciliated cells in non-infected epithelia. This latter

252   observation is consistent with previous reports showing that SARS-CoV-2 infection of lung

253   epithelial cells trigger the partial loss of cilia (27). Importantly, using EM we observe vesicular

254   inclusions within those extruded cells that contained virus particles indicating that multi-

255   nucleated infected structures actively produced viruses (Fig. 3D, black arrows).

256

Infected cells and syncytia are released into the apical BE lumen and transmit infection

258   Because cells and syncytia were extruding from the epithelium, we wondered whether infected

259   cells/syncytia could be released from the epithelium and account for the spreading of the

260   infection. To test this hypothesis, we infected epithelia from two donors for three and four days.

261   Apical washes of epithelia were performed after three and four days of infection and

262   concentrated on microscope slides *via* cytospin. After IF processing, we showed that apical

263   washes contained individual infected cells (positive for N-protein staining) but also several

264   infected syncytia, suggesting that both are indeed released into the apical epithelial lumen (Fig.

265   4A). To test the relative infectivity, apical washes were clarified of cell material by low-speed

266   centrifugation. Both the clarified supernatant and the removed cellular fraction were used to

267   infect Vero E6 cells. After 24h, cells were fixed and analyzed by IF microscopy. Inoculation with

268   the supernatant as well as the cellular fraction of the apical wash showed efficient Vero E6 cell

269   infection (data not shown). In parallel, inoculated Vero E6 cells were monitored for the

270   appearance of a virus-induced CPE. Apical wash after 4 days of epithelia infection resulted in CPE

271   within 48h whereas a comparable CPE required 72h with an apical wash resulting from a 3 days

272   infection (data not shown). AT 96h post-infection the Vero E6 cell CPE was quantified (Fig. 4B).

273   Apical washes from non-infected epithelia produced only background levels of cell death (gray

274   bars, Fig. 4B). In contrast, significant levels of cell death occurred in Vero E6 cell after inoculation

275   with either the supernatant or the pellet (cellular fraction) of an apical wash issued from an

276   infected epithelium (black bars, Fig. 4B). Taken together this analysis shows that epithelia produce

277   and release large amounts of new viruses into the apical lumen, a significant fraction of the

278   released infectious virus dose stems from infected cells and syncytia.

279

280   **Epithelia from children partially restrict SARS-CoV-2 infection but not syncytia formation**

281   In our experimental model, each epithelium can be traced to an individual donor, while generating

282   enough individual inserts to allow biological repeats and kinetic studies. Our analysis showed that

283   epithelia from several adult donors responded similarly to the infection with SARS-CoV-2. A

284   striking observation was that infections spread very fast over the entire epithelia and produced

285   vast amounts of syncytia for apical release in a synchronized manner. Adult donors in this study

286   were between 46 and 63 years old (table 1), which puts them statistically into a medium/high risk

287   group to develop severe COVID-19 symptoms. In contrast, several reports have indicated that

288   children are much less susceptible to severe forms of COVID-19, while their role in spreading virus

289   infections is controversially discussed (37, 38). To investigate whether SARS-CoV-2 infects BEs

290   differently depending on the age of donors, we prepared epithelia through expansion and

291   differentiation of bronchial epithelial cells obtained from children (Table 1) that have undergone

292   bronchial fibroscopy for chronic bronchopathy (child C1) or bronchiectasis (children C2 and C3).

293   Fully differentiated epithelia from children showed the same cellular arrangement (epithelial

294   cells, basal cells, goblet cells) and physiological properties (cilia beating, mucus production) as

295   adult derived epithelia. A kinetic experiment was performed to compare the SARS-CoV-2 infection

296   dynamics in BEs derived from children (C1 to C3) or from adult donors (A5 and A6). The BEs were

297   fixed at 1, 2, 3, 4 and 7 d.p.i. with a non-infected control for each donor run in parallel and fixed

298   at day 7. Individual epithelia were fixed and processed for IF analysis using antibodies against

299   cytokeratin 5, SARS-CoV-2 N-protein and counterstained with fluorescently labelled phalloidin

300   and DAPI. As observed before (Fig. 2), infecting BEs from adult donors at a MOI of 0.012 resulted

301   in a fast increase in the presence of infected cells (within 48h) and the formation of a significant

302 amount of syncytia on the fourth day (A6, Fig. S3A). In sharp contrast, all child derived epithelia

303 showed a remarkable resistance to virus infection (Fig. S3 B-D). Of note, virus spread differed

304 significantly in BE originating from the individual child donor. A slow but substantial increase in

305 infected cells over time was observed in BE derived from donor C1 (Fig. S3B). In comparison, BE

306 derived from C2 did not support substantially increase of the number of infected cells after the

307 initial appearance of positive cells (Fig. S3C) and BE derived from the last donor, C3, only ever

308 showed very few infected cells, reminiscent of an abortive infection (Fig. S3D). Low magnification

309 imaging of the entire epithelia showed that initial infections in BE from donor C1 were limited to

310 few cells. The N-protein associated signal seemed to grow over time into foci of infection that

311 further enlarged by infecting surrounding cells at the periphery (Fig. 5A, top row, left). High-

312 resolution images confirmed that cells at the foci border stained strongly, while several cells

313 surrounding these foci were already positive for SARS-CoV-2 N-protein. This suggested the

314 existence of a front of highly replicating cells with forward cell-to-cell or short range spread as

315 infection mode (Fig. 5B). In contrast, infection spread in epithelia from donor C2 seemed to be

316 even more restricted (Fig. 5A, bottom row, left). In the case of the BE derived from the child donor

317 C2, most of the cells that were initially infected at day one/two developed into local cluster of

318 infected cells without much lateral spread. High-resolution imaging revealed that within these

319 clusters, several cells fused with basal cells to form small syncytia that had apical localization (Fig.

320 5C, movie S9), reminiscent with what was observed in adult donors. It is only after seven days of

321 infection that some spreading into small patches could be observed, mimicking observations

322 made for C1 on the second and third day of infection. Low magnification imaging of the entire

323 epithelia derived from child C3 confirmed sporadic infection signals in the BEs, while the adult-

324 derived control A7 showed massive spread of the infection throughout the entire epithelia at 4

325 d.p.i (right panel, Fig. 5A). Quantifying the total number of infected cells in each epithelium

326 confirmed our observation (Fig. 5D). In contrast to the adult control, no significant differences in

327 signal size was observed between day three and day four for either of the children derived

328 epithelia (Fig. 5E). Still, the average signal size appeared larger likely due to clustering of infected

329 cells (Fig. 5E). For all three children derived epithelia and the adult control we also measured the

330 accumulation of SARS-CoV-2 in the apical lumen using quantitative PCR (Fig. 5F). The quantities

331 of released virus over time accurately reflected the spread of infection observed by IF and

332 quantification of infected cells. Taken together our analysis clearly demonstrated that epithelia

11

333   from children were less susceptible to SARS-CoV-2 and exhibited an intrinsic resistance towards

334   virus infection and/or spread. One possible explanation for this intrinsic resistance of children BE

335   could be differences in IFN response (39, 40) or morphological differences (41). Accordingly, we

336   compared the accumulation of interferon λ 1/3 and measured the concentration in BE medium

337   from adults and children in response to SARS-CoV-2 infection (Fig. 5G). We did not find interferon

338   λ at the beginning of the infection. Children BE secreted interferon λ starting at day 1 post-

339   infection whereas adult BE produced detectable amount of interferon λ only at day 3 post-

340   infection. Interferon λ concentration increased subsequently for both age groups and reached

341   similar levels at day 4 and 7 post-infection (Fig. 5G). The difference in the kinetic for Interferon λ

342   secretion between adults and children in response to SARS-CoV-2 infection may thus provide an

343   explanation why in our model children derived BE resist better to SARS-CoV-2 infection. Still, the

344   strength of this resistance differs from donor to donor and delays virus spread to different degrees

345   or may prevent virus spread entirely.

346
347
348   **Discussion**
349
350   In this study, we used human reconstituted bronchial epithelia to investigate the onset of

351   infection and replication of SARS-CoV-2 in BE. Our approach uses primary cells from individual

352   patients obtained through our local hospital collected in the bronchial tree between the third and

353   fifth generation. Bronchial epithelia are an important tissue to study because following initial

354   infection in the upper airways, subsequent infection of the bronchial tissue determines whether

355   a SARS-CoV-2 infection results in severe or mild respiratory illness by controlling the spread into

356   the lower respiratory tract. These features make a distinction in our approach from similar studies

357   using primary respiratory cells from either upper airway (nasal, tracheal) (3, 26) or commercial

358   sources (27) with undefined donor material. Using this physiological model, we observed SARS-

359   CoV-2 production mainly on the apical side of the epithelia following infection. We then used

360   immunofluorescence imaging to follow and compare the infection in the BE from several

361   individual donors for seven days. This approach allowed the detection of infected cells as early as

362   24h post-infection. The infection spread throughout the whole epithelia within three to four days

363   post inoculation followed by a drop in the number of infected cells on the last day. Quantification

364   of viral RNA confirmed these observations and showed that viral replication reached a plateau

365   around day four post-infection. Using cell specific markers, we identified that infected cells during

366   the first two days corresponded largely to multi-ciliated cells staining positive for acetylated

367   tubulin in agreement with previous studies (26, 28). We rarely observed infected basal or goblet

368   cells during this period. Interestingly, starting at day three of the infection not only the infected

369   cell number but also the signal size of infected cells increased with a statistically significant shift

370   towards larger cells between day three and four. We could show that the larger signals

371   corresponded to infected multinucleated syncytia. The formation of cell fusions in coronavirus

372   infected primary airway epithelia was previously reported (28, 42) but not systematically detected

373   (26, 27, 32). In our study, we were able to find extensive syncytia formation in all six adult donors.

374   Syncytia formation was transient and reached a maximum at day four to sharply drop towards

375   the seventh day. The fusogenic potential of SARS-CoV-2 is well known and involves the Spike

376   protein and the ACE2 receptor (43, 44). When we used cell specific markers to identify the syncytia

377   cell composition we found that several syncytia were double positive for the basal cell marker

378   cytokeratin 5 as well as the cilia marker acetylated tubulin or only for the basal cell marker (Fig.

379   3). This suggested that syncytia are formed by the fusion of basal cells with infected multi-ciliated

380   cells. This is consistent with previous reports that infection of multi-ciliated cells with SARS-CoV-

381   2 results in cilia loss and cell dedifferentiation (27, 28). Fusion of initially infected multi-ciliated

382   cells with basal cells as one mode of virus cell-to-cell spread was further supported by

383   quantification of infected syncytia positive for cytokeratin 5, which constantly increased in

384   number until day four in all analyzed donors. The sharp drop on day four in the number of double

385   positive syncytia, but not in the number of overall infected cells, is consistent with our observation

386   that syncytia were extruded at the apical side of the epithelia. We found frequent syncytia

387   forming at the apical side of the epithelia positive for the N nucleoprotein and EM analysis showed

388   that they indeed contained high amounts of virus trapped in a vesicular compartment.

389   Furthermore, we were able to show that infected syncytia are released into the apical supernatant

390   and that released syncytia and infected cells are as infectious as free virus (Fig. 4). This strongly

391   suggests that infected syncytia and cell release into the apical lumen could be an important

392   contribution to the spreading of large and compact amounts of viruses into the upper respiratory

393   tract from which cell associated virus can either decent into the lower respiratory tract or reach

394   the environment increasing the actual infectious dose. Interestingly, pathology reports from

395   patients succumbed to Covid-19 show abnormal syncytia formed by pneumocytes in the lower

396 respiratory tract suggesting that our observations in the BE model find their counterpart in severe

397 forms of COVID-19 (14, 45, 46). Accordingly, such an event would be in agreement with the clinical

398 observation of hospitalized patients, which reported a high detection of SARS-CoV-2 in sputum

399 and its transmission by droplets (19). The fact that syncytia production is massive but transient is

400 well correlated with another report showing that virus production in a primary airway epithelium

401 is cyclic with peaks of virus release every 7-10 days (26). The authors suggest that this periodicity

402 is driven by recurrent epithelia removal and regeneration. Interestingly, such a peak in virus

403 production would provide an explanation for the phenomenon of "super spreader", frequently

404 suggested based on epidemiological data (47). A periodicity or variability in the quantity of virus

405 released from infected tissue thus may affect contagion. Furthermore, we also observed the loss

406 of cilia in many of the syncytia, which could be responsible for a poor mucociliary clearance that

407 impedes the evacuation of viral particles and pathogens. Taken together, our findings are in

408 accordance with previous findings but highlight syncytium formation as an important mechanism

409 to explain the spreading of SARS-CoV-2 and the physiopathology of bronchial epithelium infection

410 (14, 43, 45, 46). Since the beginning of the COVID-19 pandemic, SARS-CoV-2 infection is more

411 virulent in adults compared to children. We explored the bronchial epithelium infection of

412 children with SARS-CoV-2 and compared our observations with those made in BE from adult

413 donors. Strikingly, we find very different spreading of SARS-CoV-2 in children BE *versus* adult BE.

414 First, the overall viral production was very low in BE of children compared to adults, which is

415 reflecting the slower kinetic in the onset of virus production over time. In agreement with the

416 virus quantification, child epithelia showed a remarkable resistance to virus infection as very few

417 infected cells were observed. Rather than rapidly spreading throughout the entire epithelia, as

418 observed for adults, the infected cells in children form cluster or foci of infected cells. From these

419 foci, the infection slowly spread into the surrounding bystander cells. Yet, syncytia formation was

420 also observed, at least in one child, suggesting that the fusion of basal cells with multi-ciliated

421 cells was not restricted to adult infected BE. However, the number of syncytia was much lower

422 than in adults reflecting the low virus spread. The obvious difference in susceptibility to SARS-

423 CoV-2 infection between adults and children, which we observed in the BE model is in agreement

424 with the reduced epidemiological infection rate described for children and strong discrepancy in

425 death rate between children and adults/elderly (24, 25). A very recent study using nasal BE also

426 showed differences in the susceptibility to SARS-CoV-2 infection between adults and children (32).

427   The reason for this intrinsic difference between adults and children BE is unknown. One possible

428   explanation could be an age-related variation in the expression or accessibility of the primary viral

429   receptors (ACE2 and TMPRSS2) (48). We show that children BE have a quicker induction of

430   interferon λ in response to SARS-CoV-2 infection starting as soon as 1-day post-infection whereas

431   adults BE exhibit detectable level of interferon λ only 3-day post-infection. Recent studies show

432   that SARS-CoV-2 blocks the interferon response by targeting the RIG-I/MDA-5 pathway (49, 50).

433   Our study is consistent with a delay of Interferon λ production after SARS-CoV-2 infection in adults

434   but less so in children. This could suggest that either SARS-CoV-2 is less efficient in counteracting

435   the IFN response in children BE or alternatively, that the IFN response in children is faster and an

436   antiviral state is induced throughout the epithelia that slows down virus spread. Such an age-

437   related susceptibility of BE has been reported for other respiratory pathogens including

438   respiratory viruses such as Rhinovirus-C, Adenovirus and RSV (Respiratory Syncytial Virus) (51,

439   52)(53) but also fungi (Aspergillus fumigatus) (54) and bacteria (Haemophilus influenzae) (55).

440   Future studies will be required to study the exact mechanism behind the differences in IFN

441   response that we observed. Taken together our data clearly demonstrate that BE from children

442   are less susceptible to SARS-CoV-2 infection. Our data suggest that an accelerated interferon

443   response might contribute to this resistance supporting timed interferon application as

444   therapeutically beneficial concept in the treatment of SARS-CoV-2 infections (56-58).

445

446   **Materials and Methods**

447

448   **Monoclonal antibodies and ethics statement**

449   Monoclonal antibodies were raised against bacterially expressed and purified SARS-CoV-2 N

450   protein in 3 mice using the protocol as previously described (59). Hybridomas were cloned by

451   limiting dilution and screened by immunofluorescence on infected VERO cells. Clone 3G9 was

452   retained for this study and antibody was affinity purified from hybridoma supernatant prior to

453   use. Mice experiments have been performed in the conventional animal facilities of the University

454   of Bordeaux (France) (approval number of B-33-036-917), with the approval of institutional

455   guidelines determined by the local Ethical Committee of the University of Bordeaux and in

456 conformity with the Ministry for Higher Education and Research and the French Committee of

457 Genetic Engineering (approval number n °17621 -V5- 2018112201234223).

Viruses and cell lines

459 Vero E6 cells were maintained in Dulbecco's modified Eagle's medium (DMEM, Gibco)

460 supplemented with 10% fetal calf serum (FCS) and gentamicin (50µg/mL) at 37°C in a humidified

461 CO_2 incubator. The SARS-CoV-2 strain BetaCoV/France/IDF0372/2020 was supplied by the

462 National Reference Centre for Respiratory Viruses hosted by Pasteur Institute (Paris, France)

463 through the European Virus Archive goes Global (EVAg platform). Agreement to work with

464 infectious SARS-CoV-2 was obtained and all work with infectious SARS-CoV-2 was performed in a

465 Class II Biosafety Cabinet under BSL-3 conditions at the UB'L3 facility (TBM core, Bordeaux).

Viral production

467 The SARS-CoV-2 strain was produced by infecting Vero E6 cells at a multiplicity of infection (MOI)

468 of 0.01, then incubating the cells at 37°C in a humidified CO_2 incubator until appearance of a

469 cytopathic effect (around 72 h). The culture supernatant was clarified by centrifugation (5 minutes

470 at 1500 rpm) and aliquots were stored at −80°C. Stock titers were determined by adding serial

471 dilutions to 2×10^4 Vero E6 cells in supplemented DMEM in a 96-well plate. Eight replicates were

472 performed. Plates were incubated at 37°C and examined for cytopathic effect. Quantification of

473 cytopathic effect was determined using the Cell tox ^{TM} green cytotoxicity assay (Promega)

474 according to manufacturer instructions and a Victor Nivo reader (Perkin Elmer). The $TCID_{50}$ was

475 calculated according to the method of Reed & Muench (60). PFU/ml was estimated from the

476 $TCID_{50}$ determination.

Culture of primary bronchial epithelia (BE) and ethics statement

478 Bronchial epithelial cell culture was established from bronchial brushings or lung resection

479 performed between the third and fifth bronchial generation from patients undergoing elective

480 surgery as previously described (34). Bronchial epithelium explants were cultured using

481 PneumaCult Ex medium (Stemcell, Vancouver, Canada) for expansion of basal epithelial cells at

482 37°C in 5% CO_2. Then, 10^5 basal cells were grown on cell culture inserts (Corning, New York, NY)

16

483   within the air-liquid interface for 21 days using PneumaCult ALI medium (Stemcell, Vancouver,

484   Canada). Such a culture allows the differentiation into pseudostratified muco-ciliary airway

485   epithelium composed of ciliated cells, goblet cells, club cells and basal cells. The complete

486   differentiation was assessed by the capacity of cilia to beat and mucus production under light

487   microscope. The study received approval from the local and national ethics committee from the

488   CNIL through the TUBE collections.

489   **Infection of epithelia**

490   Prior to infection, epithelia were washed three times with PBS to remove mucus and basal ALI

491   medium was exchanged with 500 μL of fresh medium. The inoculum containing 1200 PFU of virus

492   or medium-only controls were added to the apical surface to a final volume of 100 μL. Viral

493   supernatant was removed after 1 hour incubation at 37°C and infection was followed for the

494   indicated time points. Viral production was then quantified by qRT-PCR using 3 consecutively

495   collected apical washes of 100 μL PBS.

496   **Quantification of SARS-CoV-2 RNA by qRT-PCR**

497   For quantification of viral RNA by qRT-PCR, total RNA was isolated using the High Pure Viral RNA

498   kit (Roche) according to the manufacturer's instruction. Viral RNA was quantified using GoTaq® 1-

499   Step RT-qPCR kit (Promega). SARS-CoV-2 N gene RNA was amplified using forward (Ngene F

500   cgcaacagttcaagaaattc 28844-28864) and reverse primers (Ngene R ccagacattttgctctcaagc 28960-

501   28981). Copy numbers were calculated from a standard curve produce with serial 10-fold dilutions

502   of SARS-CoV-2-RNA. Amplification program began with the RT-step 15 min at 50°C then the

503   denaturation step 10 min at 95°C, and 10 s at 95°C, 10 s at 60°C and 10 s at 72°C (40 cycles). The

504   melting curve was obtained by temperature increment 0,5°C/s from 60°C to 95°C.

505   **Interferon ELISA**

506   Human IL-29/IL-28B (IFN-lambda 1/3) concentration in SARS-CoV-2 infected epithelium basal

507   media was quantified using ELISA technics following manufacturer's recommendations (R&D

508   systems, Minneapolis, USA). 100 μl of media was used for each point.

509   **Immunofluorescence detection, antibodies and confocal microscopy.**

17

510   For antigen detection, BE were washed repeatedly with PBS to remove mucus then fixed with 4%

511   paraformaldehyde for 30min using complete insert immersion. Epithelia were then washed and

512   permeabilized with 0.5% TritonX-100 in PBS for 10min at room temperature and blocked in IF

513   buffer (PBS containing 10% SVF and 0.5% saponin) for 1h at room temperature. Primary antibody

514   and fluorescently labeled phalloidin to stain the actin cytoskeleton was diluted in IF buffer and

515   applied to inserts for 1h at room temperature. Samples were washed three times under agitation

516   with PBS and incubated with secondary antibody diluted in IF buffer and incubated for 2h at room

517   temperature. Insert were then washed in PBS, desalted in H_2O miliQ and rinsed in Ethanol 100%

518   and air-dried. Membranes were then removed from inserts and mounted in DAPI (4',6-diamidino-

519   2-phenylindole) containing DAKO Fluorescence Mounting Medium prior to microscopy analysis.

520   Mounted samples were subsequently examined on an epifluorescence microscope (Leica inverted

521   DRMi6000 widefield microscope) at low resolution for kinetic studies. High resolution analysis

522   was performed on a SP8 confocal microscope (Leica Microsystems at the Bordeaux Imagery

523   center) using maximal pixel resolution at 20x, 40x or 63x respectively and 0.3µm Z-stacks

524   resolution. Full epithelia overviews were acquired with Leica LAS-X software in spiral mosaics

525   mode and three-dimensional reconstructions were done with Leica LAS-X software in 3D-viewer

526   mode. Image processing was done using Image J software. Signal of interest were quantified using

527   a semi-automatic macro. Briefly, Z-projections of different focal planes were generated and

528   regions of interest (ROI) were manually inserted. Signal of interest was quantified automatically

529   in each ROI, with appropriate predefined threshold and sizing for each condition. Quantification

530   were performed to measured either number or size of signal of interest. Obtained values are

531   represented either as absolute number or as normalized values (as indicated). The following

532   primary antibodies and IF dilutions were used in this study; mouse monoclonal Ab anti-SARS-CoV-

533   2-N clone 3G9 (this study, 1:500), rabbit monoclonal Ab anti-human Cytokeratin 5 (Abcam,

534   ab52635, 1:200), rabbit polyclonal Ab anti-human Acetylated tubulin (Cell Signaling, D20G3,

535   1:200), rabbit polyclonal Ab anti-human ACE2 (Abcam, ab15348, 1:50), rabbit monoclonal Ab anti-

536   human-Mucin 5AC (Abcam, ab198294, 1:200). The following secondary antibodies were used in

537   this study; cross absorbed Donkey anti-mouse Alexa Fluor 488 or 647 (Life technologies,

538   A212020/A31571, 1:300) and cross absorbed Donkey anti-rabbit Alexa Fluor 594 (Life

539   technologies, A31573, 1:300) as well as Alexa-Fluor 594 labeled phalloidin (Invitrogen, 1:500).

Electron microscopy

541 For electron microscopy, epitheliums were first washed in physiological serum and then fixed with
542 2.5% (v/v) glutaraldehyde and 2% (v/v) paraformaldehyde in 0.1M phosphate buffer (pH 7.4)
543 during 2h minimum at room temperature (RT). Then samples were washed in 0.1M phosphate
544 buffer and post-fixed in 1% (v/v) osmium tetroxide in phosphate buffer 0.1 M during 2h, in the
545 dark, at RT, then washing in water and dehydrated through a series of graded ethanol and
546 embedded in a mixture of pure ethanol and epoxy resin (Epon 812; Delta Microscopy, Toulouse,
547 France) 50/50 (v/v) during 2 hours and then in 100% resin overnight at RT. The polymerization of
548 the resin was carried out over a period between 24-48 hours at 60°C. Samples were then
549 sectioned using a diamond knife (Diatome, Biel-Bienne, Switzerland) on an ultramicrotome (EM
550 UCT, Leica Microsystems, Vienna, Austria). Ultrathin sections (70 nm) were picked up on copper
551 grids and then stained with uranyless and lead citrate. Grids were examined with a Transmission
552 Electron Microscope (H7650, Hitachi, Tokyo, Japan) at 80kV.

References

570   1.   N. S. Zhong *et al.*, Epidemiology and cause of severe acute respiratory syndrome (SARS)
571   in Guangdong, People's Republic of China, in February, 2003. *Lancet* **362**, 1353-1358
572   (2003).
573   2.   J. Cui, F. Li, Z. L. Shi, Origin and evolution of pathogenic coronaviruses. *Nature reviews.*
574   *Microbiology* **17**, 181-192 (2019).
575   3.   N. Zhu *et al.*, A Novel Coronavirus from Patients with Pneumonia in China, 2019. *The New*
576   *England journal of medicine* **382**, 727-733 (2020).
577   4.   P. Zhou *et al.*, A pneumonia outbreak associated with a new coronavirus of probable bat
578   origin. *Nature* **579**, 270-273 (2020).
579   5.   F. Wu *et al.*, A new coronavirus associated with human respiratory disease in China.
580   *Nature* **579**, 265-269 (2020).
581   6.   R. Cannalire, C. Cerchia, A. R. Beccari, F. S. Di Leva, V. Summa, Targeting SARS-CoV-2
582   Proteases and Polymerase for COVID-19 Treatment: State of the Art and Future
583   Opportunities. *Journal of medicinal chemistry* 10.1021/acs.jmedchem.0c01140 (2020).
584   7.   P. V'Kovski, A. Kratzel, S. Steiner, H. Stalder, V. Thiel, Coronavirus biology and replication:
585   implications for SARS-CoV-2. *Nature reviews. Microbiology* **19**, 155-170 (2021).
586   8.   J. F. Chan *et al.*, Genomic characterization of the 2019 novel human-pathogenic
587   coronavirus isolated from a patient with atypical pneumonia after visiting Wuhan.
588   *Emerging microbes & infections* **9**, 221-236 (2020).
589   9.   M. Hoffmann *et al.*, SARS-CoV-2 Cell Entry Depends on ACE2 and TMPRSS2 and Is Blocked
590   by a Clinically Proven Protease Inhibitor. *Cell* **181**, 271-280.e278 (2020).
591   10. N. Clementi *et al.*, Viral Respiratory Pathogens and Lung Injury. *Clinical microbiology*
592   *reviews* **34** (2021).
593   11. S. Tian *et al.*, Pulmonary Pathology of Early-Phase 2019 Novel Coronavirus (COVID-19)
594   Pneumonia in Two Patients With Lung Cancer. *Journal of thoracic oncology : official*
595   *publication of the International Association for the Study of Lung Cancer* **15**, 700-704
596   (2020).
597   12. S. Tian *et al.*, Pathological study of the 2019 novel coronavirus disease (COVID-19) through
598   postmortem core biopsies. *Modern pathology : an official journal of the United States and*
599   *Canadian Academy of Pathology, Inc* **33**, 1007-1014 (2020).
600   13. A. C. Borczuk, Pulmonary pathology of COVID-19: a review of autopsy studies. *Current*
601   *opinion in pulmonary medicine* **27**, 184-192 (2021).
602   14. R. Bussani *et al.*, Persistence of viral RNA, pneumocyte syncytia and thrombosis are
603   hallmarks of advanced COVID-19 pathology. *EBioMedicine* **61**, 103104 (2020).
604   15. M. Liao *et al.*, Single-cell landscape of bronchoalveolar immune cells in patients with
605   COVID-19. *Nature medicine* **26**, 842-844 (2020).
606   16. C. Huang *et al.*, Clinical features of patients infected with 2019 novel coronavirus in
607   Wuhan, China. *Lancet* **395**, 497-506 (2020).
608   17. B. Rockx *et al.*, Comparative pathogenesis of COVID-19, MERS, and SARS in a nonhuman
609   primate model. *Science (New York, N.Y.)* **368**, 1012-1015 (2020).
610   18. B. Hu, H. Guo, P. Zhou, Z. L. Shi, Characteristics of SARS-CoV-2 and COVID-19. *Nature*
611   *reviews. Microbiology* **19**, 141-154 (2021).
612   19. R. Wölfel *et al.*, Virological assessment of hospitalized patients with COVID-2019. *Nature*
613   **581**, 465-469 (2020).
614   20. H. Kawasuji *et al.*, Transmissibility of COVID-19 depends on the viral load around onset in
615   adult and symptomatic patients. *PloS one* **15**, e0243597 (2020).

21. L. Zou *et al.*, SARS-CoV-2 Viral Load in Upper Respiratory Specimens of Infected Patients. *The New England journal of medicine* **382**, 1177-1179 (2020).

22. J. Wu *et al.*, Identification of RT-PCR-Negative Asymptomatic COVID-19 Patients via Serological Testing. *Frontiers in public health* **8**, 267 (2020).

23. X. Lu *et al.*, SARS-CoV-2 Infection in Children. *The New England journal of medicine* **382**, 1663-1665 (2020).

24. B. Salzberger *et al.*, Epidemiology of SARS-CoV-2. *Infection* **49**, 233-239 (2021).

25. E. Goldstein, M. Lipsitch, M. Cevik, On the Effect of Age on the Transmission of SARS-CoV-2 in Households, Schools, and the Community. *The Journal of infectious diseases* **223**, 362-369 (2021).

26. S. Hao *et al.*, Long-Term Modeling of SARS-CoV-2 Infection of In Vitro Cultured Polarized Human Airway Epithelium. *mBio* **11** (2020).

27. M. H. Rémy Robinot, Guilherme Dias de Melo, Françoise Lazarini, Timothée Bruel, Nikaïa Smith, Sylvain Levallois, Florence Larrous, Julien Fernandes, Stacy Gellenoncourt, Stéphane Rigaud, Olivier Gorgette, Catherine Thouvenot, Céline Trébeau, Adeline Mallet, Guillaume Duménil, Samy Gobaa, Raphaël Etournay, Pierre-Marie Lledo, Marc Lecuit, Hervé Bourhy, Darragh Duffy, Vincent Michel, Olivier Schwartz, Lisa A. Chakrabarti, 10.1101/2020.10.06.328369

28. N. Zhu *et al.*, Morphogenesis and cytopathic effect of SARS-CoV-2 infection in human airway epithelial cells. *Nature communications* **11**, 3910 (2020).

29. D. Blanco-Melo *et al.*, Imbalanced Host Response to SARS-CoV-2 Drives Development of COVID-19. *Cell* **181**, 1036-1045.e1039 (2020).

30. J. Hadjadj *et al.*, Impaired type I interferon activity and inflammatory responses in severe COVID-19 patients. *Science (New York, N.Y.)* **369**, 718-724 (2020).

31. Q. Zhang *et al.*, Inborn errors of type I IFN immunity in patients with life-threatening COVID-19. *Science (New York, N.Y.)* **370** (2020).

32. S. L. W. Alexander Capraro, Anurag Adhikari, Katelin M Allan, Hardip R Patel, Ling Zhong, Mark Raftery, Adam Jaffe, Malinna Yeang, Anupriya Aggarwal, Lindsay Wu, Elvis Pandzic, Renee M Whan, Stuart Turville, Orazio Vittorio, Rowena A Bull, View Nadeem Kaakoush, VWilliam D Rawlinson, Nicodemus Tedla, VFatemeh Vafaee, Shafagh A Waters, 10.1101/2021.04.05.437453.

33. B. Allard *et al.*, Asthmatic Bronchial Smooth Muscle Increases CCL5-Dependent Monocyte Migration in Response to Rhinovirus-Infected Epithelium. *Frontiers in immunology* **10**, 2998 (2019).

34. T. Trian *et al.*, House dust mites induce proliferation of severe asthmatic smooth muscle cells via an epithelium-dependent pathway. *American journal of respiratory and critical care medicine* **191**, 538-546 (2015).

35. I. T. Lee *et al.*, ACE2 localizes to the respiratory cilia and is not increased by ACE inhibitors or ARBs. *Nature communications* **11**, 5453 (2020).

36. X. Xie *et al.*, An Infectious cDNA Clone of SARS-CoV-2. *Cell host & microbe* **27**, 841-848.e843 (2020).

37. J. Bullard *et al.*, Infectivity of severe acute respiratory syndrome coronavirus 2 in children compared with adults. *CMAJ : Canadian Medical Association journal = journal de l'Association medicale canadienne* **193**, E601-e606 (2021).

660 38. Z. Hyde, Difference in SARS-CoV-2 attack rate between children and adults may reflect
661   bias. *Clinical infectious diseases : an official publication of the Infectious Diseases Society*
662   *of America* 10.1093/cid/ciab183 (2021).
663 39. M. L. Stanifer, C. Guo, P. Doldan, S. Boulant, Importance of Type I and III Interferons at
664   Respiratory and Intestinal Barrier Surfaces. *Frontiers in immunology* **11**, 608645 (2020).
665 40. S. Triana *et al.*, Single-cell analyses reveal SARS-CoV-2 interference with intrinsic immune
666   response in the human gut. *Molecular systems biology* **17**, e10232 (2021).
667 41. S. L. Lee, C. O'Callaghan, Y. L. Lau, C. D. Lee, Functional analysis and evaluation of
668   respiratory cilia in healthy Chinese children. *Respiratory research* **21**, 259 (2020).
669 42. A. C. Sims *et al.*, Severe acute respiratory syndrome coronavirus infection of human
670   ciliated airway epithelia: role of ciliated cells in viral spread in the conducting airways of
671   the lungs. *Journal of virology* **79**, 15511-15524 (2005).
672 43. J. Buchrieser *et al.*, Syncytia formation by SARS-CoV-2-infected cells. *The EMBO journal*
673   **40**, e107405 (2021).
674 44. G. Papa *et al.*, Furin cleavage of SARS-CoV-2 Spike promotes but is not essential for
675   infection and cell-cell fusion. *PLoS pathogens* **17**, e1009246 (2021).
676 45. L. Braga *et al.*, Drugs that inhibit TMEM16 proteins block SARS-CoV-2 spike-induced
677   syncytia. *Nature* 10.1038/s41586-021-03491-6 (2021).
678 46. Z. Zeng *et al.*, Pulmonary pathology of early-phase COVID-19 pneumonia in a patient with
679   a benign lung lesion. *Histopathology* **77**, 823-831 (2020).
680 47. R. A. Stein, Super-spreaders in infectious diseases. *International journal of infectious*
681   *diseases : IJID : official publication of the International Society for Infectious Diseases* **15**,
682   e510-513 (2011).
683 48. B. A. Schuler *et al.*, Age-determined expression of priming protease TMPRSS2 and
684   localization of SARS-CoV-2 in lung epithelium. *The Journal of clinical investigation* **131**
685   (2021).
686 49. S. J. Oh, O. S. Shin, SARS-CoV-2 Nucleocapsid Protein Targets RIG-I-Like Receptor
687   Pathways to Inhibit the Induction of Interferon Response. *Cells* **10** (2021).
688 50. Y. Zheng *et al.*, Severe acute respiratory syndrome coronavirus 2 (SARS-CoV-2) membrane
689   (M) protein inhibits type I and III interferon production by targeting RIG-I/MDA-5
690   signaling. *Signal transduction and targeted therapy* **5**, 299 (2020).
691 51. D. W. Cox *et al.*, Human rhinovirus species C infection in young children with acute wheeze
692   is associated with increased acute respiratory hospital admissions. *American journal of*
693   *respiratory and critical care medicine* **188**, 1358-1364 (2013).
694 52. Y. Mandelia *et al.*, Dynamics and predisposition of respiratory viral co-infections in
695   children and adults. *Clinical microbiology and infection : the official publication of the*
696   *European Society of Clinical Microbiology and Infectious Diseases* **27**, 631.e631-631.e636
697   (2021).
698 53. J. Bizzintino *et al.*, Association between human rhinovirus C and severity of acute asthma
699   in children. *The European respiratory journal* **37**, 1037-1042 (2011).
700 54. C. Wojnarowski *et al.*, Sensitization to Aspergillus fumigatus and lung function in children
701   with cystic fibrosis. *American journal of respiratory and critical care medicine* **155**, 1902-
702   1907 (1997).
703 55. X. Fan *et al.*, Epidemiological analysis and rapid detection by one-step multiplex PCR assay
704   of Haemophilus influenzae in children with respiratory tract infections in Zhejiang
705   Province, China. *BMC infectious diseases* **18**, 414 (2018).

706   56.   A. A. Salman, M. H. Waheed, A. A. Ali-Abdulsahib, Z. W. Atwan, Low type I interferon
707   response in COVID-19 patients: Interferon response may be a potential treatment for
708   COVID-19. *Biomedical reports* **14**, 43 (2021).
709   57.   E. Andreakos, S. Tsiodras, COVID-19: lambda interferon against viral load and
710   hyperinflammation. *EMBO molecular medicine* **12**, e12465 (2020).
711   58.   N. Wang *et al.*, Retrospective Multicenter Cohort Study Shows Early Interferon Therapy Is
712   Associated with Favorable Clinical Responses in COVID-19 Patients. *Cell host & microbe*
713   **28**, 455-464.e452 (2020).
714   59.   R. Martinez *et al.*, The amphipathic helix of adenovirus capsid protein VI contributes to
715   penton release and postentry sorting. *Journal of virology* **89**, 2121-2135 (2015).
716   60.   L. J. REED, H. MUENCH, A SIMPLE METHOD OF ESTIMATING FIFTY PER CENT
717   ENDPOINTS12. *American Journal of Epidemiology* **27**, 493-497 (1938).

718
719

720

721

722

723   **Figures and Tables**

724

725   5 Figures, 3 supplemental Figures, 1 Table

726

727

728

24
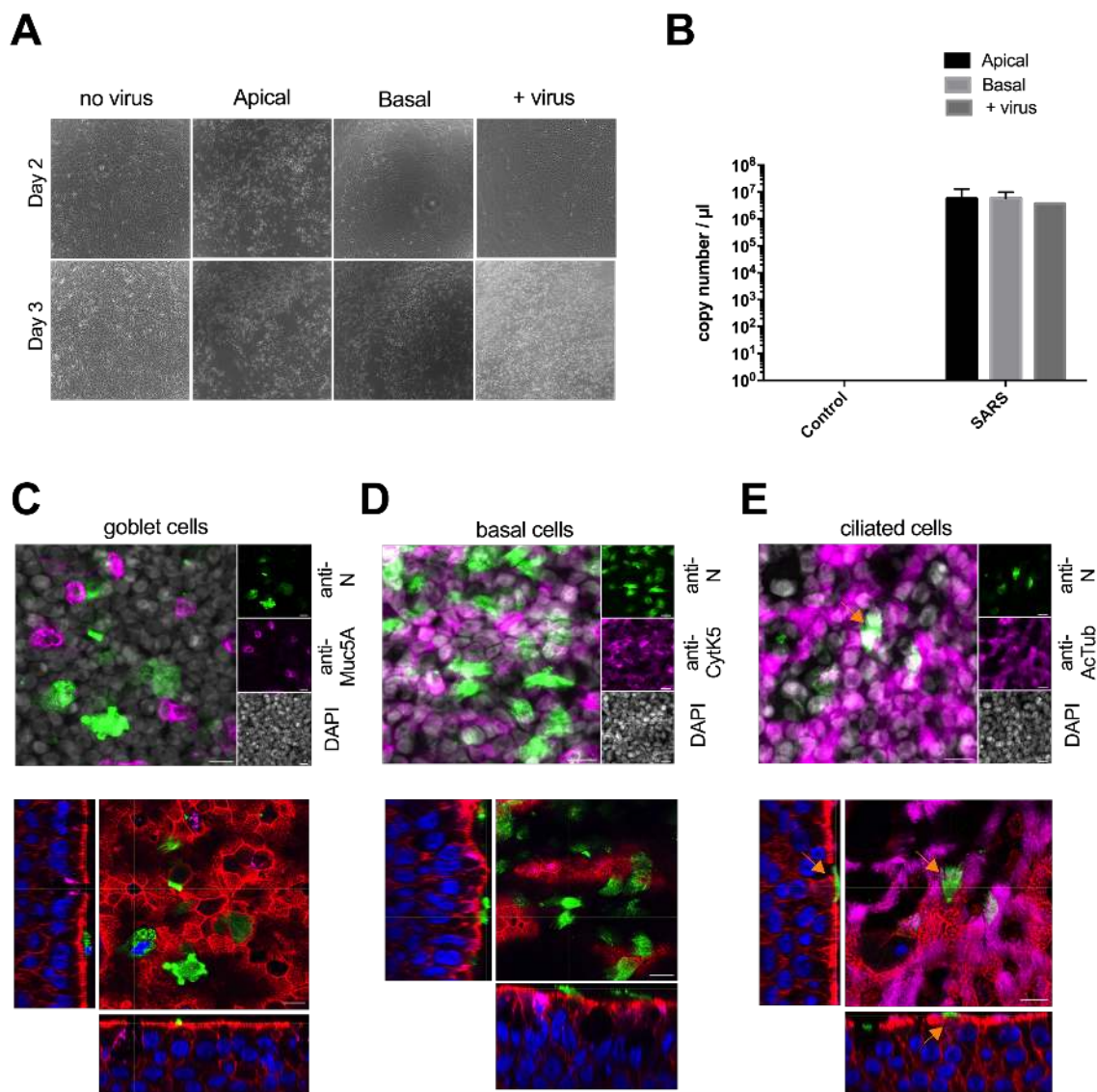
729   **Figure 1.** SARS-CoV-2 infection of bronchial epithelia (BE). A: The left panel shows brightfield
730   microscopy images of Vero E6 cells at either day 2 (top row) or day 3 (bottom row) post-inoculation
731   with apical washes, basolateral media or a viral suspension (MOI of 0.01). B: Quantification of
732   SARS-CoV-2 RNA in Vero E6 supernatant. Total RNA were extracted 96h post-infection and
733   quantified by qRT-PCR. Mean and standard deviation are derived from 3 independent
734   determinations except for the positive control (Vero E6 infected directly with a viral suspension
735   instead of BE fractions). C: Differentiated BE were infected with SARS-CoV-2 and stained 24h
736   post-infection with anti-N (green signal) to identify infected cells and anti-Muc5A to detect goblet
737   cells (magenta signal) and counterstained with DAPI (grey signal). Top image shows a Z-projection,
738   the bottom image shows an individual Z-section of a 3D reconstruction counterstained with
739   phalloidin. Scale bar is 10µm, for full Z-stack see movie S4. D: Experiment and presentation as in
740   (B) stained with anti-N (green signal) to identify infected cells and anti-cytokeratin 5 to identify basal
741   cells (magenta signal) and counterstained with DAPI (grey signal). Scale bar is 10µm, for full Z-
742   stack see movie S5. E: Experiment and presentation as in (B) stained with anti-N (green signal) to
743   identify infected cells and anti-acetylated tubulin to identify multiciliated cells (magenta signal) and
744   counterstained with DAPI (grey signal). Scale bar is 10µm, for full Z-stack see movie S6.
745
746
747   <insert page break here>

748
749

26
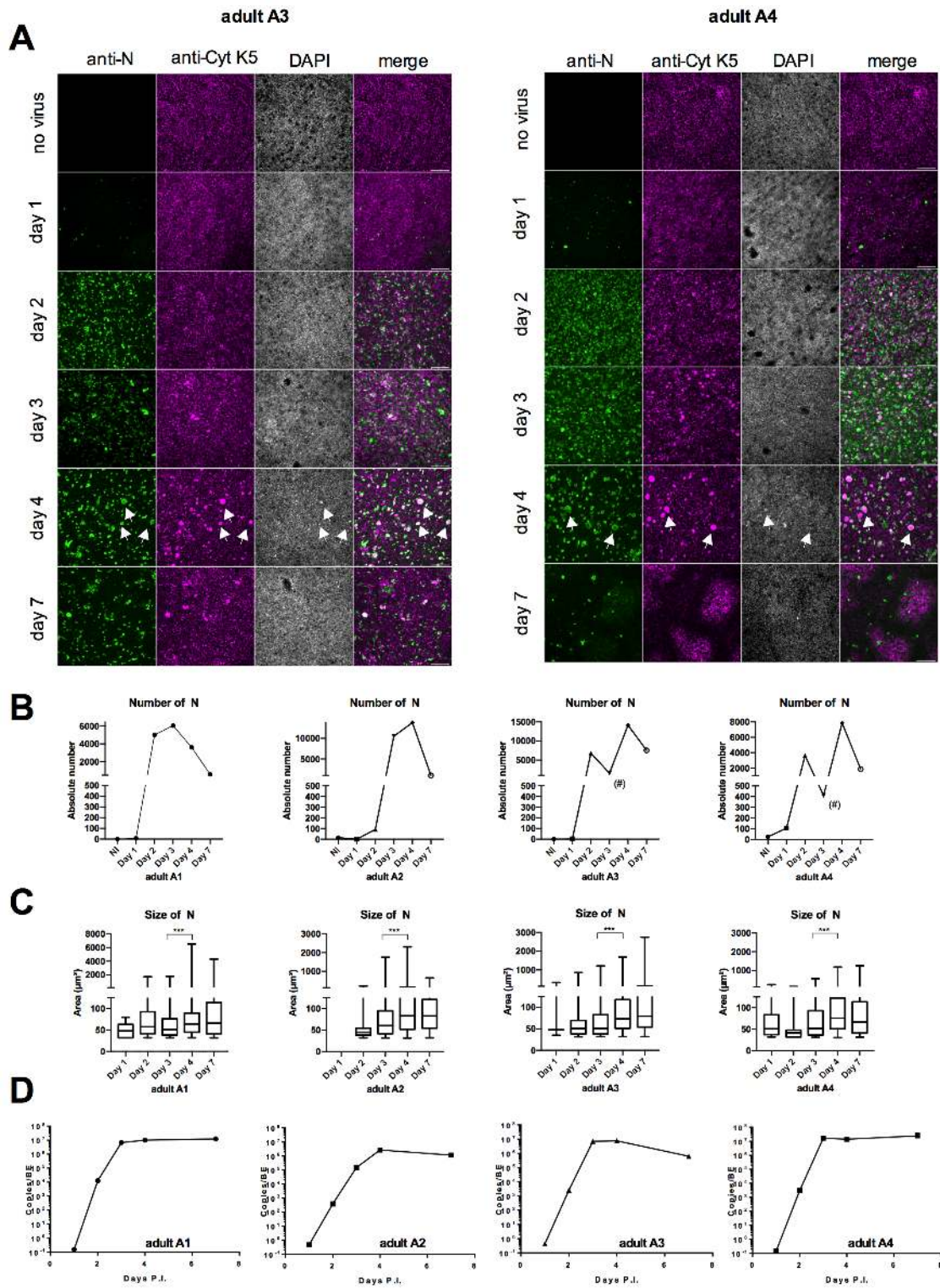
Figure 2. SARS-CoV-2 infection kinetic of bronchial epithelia (BE). A: Representative widefield microscopy images of BE from two adult donors (A3 left panel, A4 right panel) at low resolution. Scale bar is 20µm. BE were fixed at day 1, 2, 3, 4, 7 as indicated to the left of each row, non-infected controls were also fixed at day 7. BE were stained with anti-N antibodies to detect infected cells (green signal first column), anti-cytokeratin 5 to detect basal cells (magenta signal, second column) and counterstained with DAPI (grey signal, third column) and a merge of the three signals (forth column). Large specific signals in all channels are apparent on day four (white arrows). B: The absolute number of N-positive signals was determined for each BE for the whole epithelia on each day as indicated. Data shown are absolute number of N dots quantification at different days post-infection and described in material and methods. The (#) sign marks points with partial BE damage C: Signals quantified in (B) were classed by size and plotted as min to max Box & Whisker plots, *** : P< 0.001 based on One way ANOVA. D: Apical washes for each BE were subject to RT-qPCR analysis to determine genome copy numbers at day 1, 2, 3, 4, and 7 post-infection as indicated.

<insert page break here>

27

768
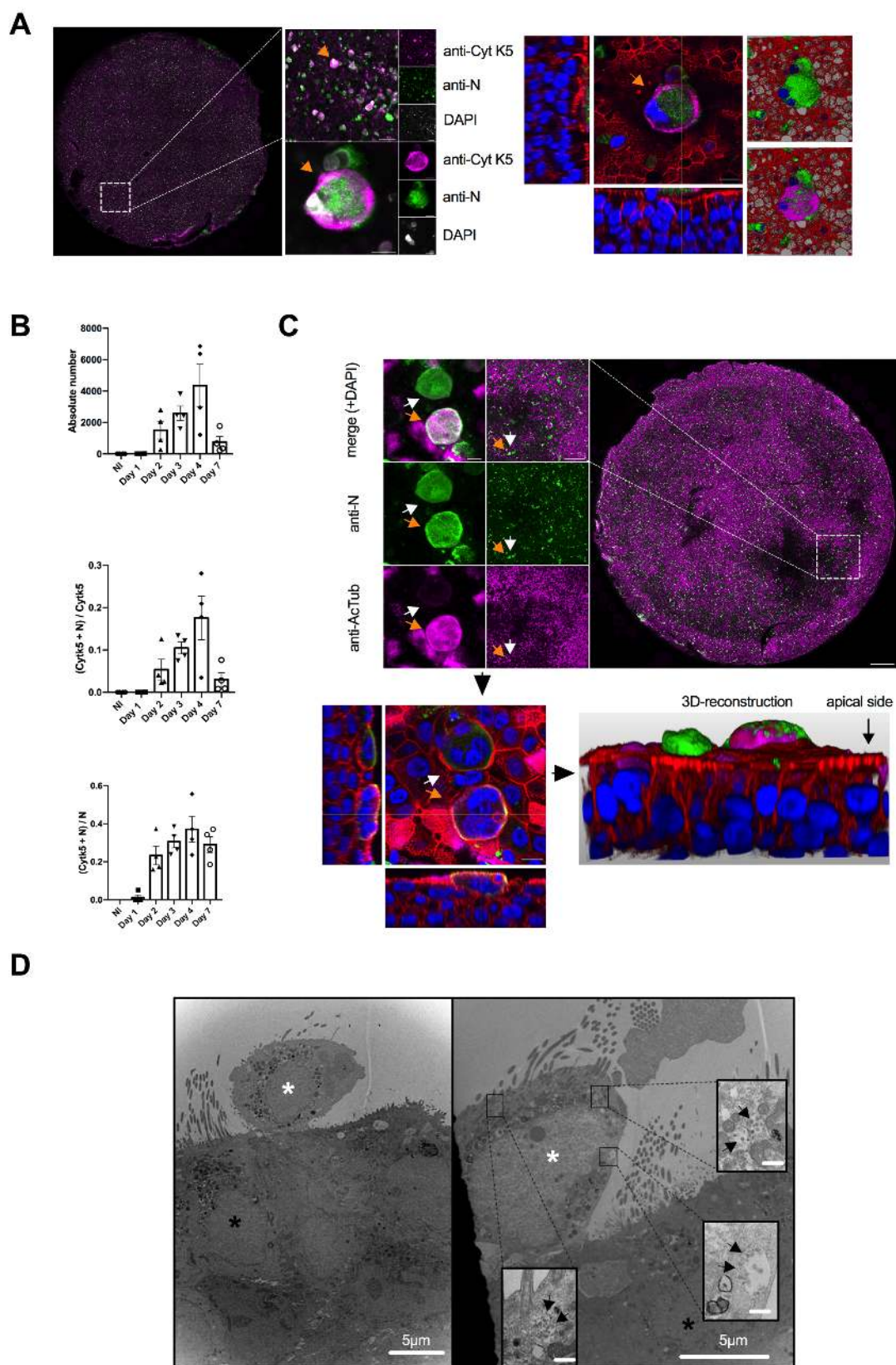
769 **Figure 3.** SARS-CoV-2 infection of bronchial epithelia (BE) induces apical syncytia. A: High
770 resolution image analysis of entire BE 4 days post-infection (left panel, adult A4). BE were stained
771 with anti-N antibodies to detect infected cells (green signal) and anti-cytokeratin 5 marking basal
772 cells (magenta signal) and counterstained with DAPI (grey signal in the left panel, blue on the right
773 panel). The boxed inset is magnified and one individual syncytia is indicated by the orange arrow.
774 The syncytia is further magnified as maximum Z-projection (left) or as individual Z-stack (right, with
775 phalloidin counterstain in red), or as 3D image reconstruction to see its apical location. Scale bar
776 is 10µm, 50µm, 200µm respectively. See also movie S7. B: Estimation of the total number of double
777 positive (N and cytokeratin 5) was determined (top panel) and normalized for total number of basal
778 cells (middle panel) and total number of infected cells (bottom panel). Data shown are absolute
779 number of colocalisations between N and cytokeratin 5 for four different donors, as determined
780 using semi-automatic quantification. Absolute number of colocalisation was then normalized by
781 absolute number of cytokeratin 5 or N positive cells. Data are presented as mean ± SD, n = 4. C:
782 High resolution image analysis of entire BE 4 days post-infection. Experiment and image
783 representation as in (A). BE were stained with anti-N antibodies to detect infected cells (green
784 signal) and anti-acetylated tubulin detecting multi-ciliated cells (magenta signal) and counterstained
785 with DAPI (grey signal in the top panel, blue on the bottom panel). Double positive syncytia are
786 marked by orange arrow, single positive syncytia with white arrow. Scale bar is 10µm, 50µm,
787 200µm respectively. See also movie S8. D: Electron micrograph of infected BE 4 days post-
788 infection. The large images show extruded cell on the apical side of the epithelia (white asterisk)
789 adjacent to multi ciliated cells (black asterisk). The insets show virus containing vacuoles in the
790 extruded cell as indicated by black arrows. Scale bars are provided in the image (5µm for large
791 images and 200nm for insert images).
792
793 <insert page break here>

794
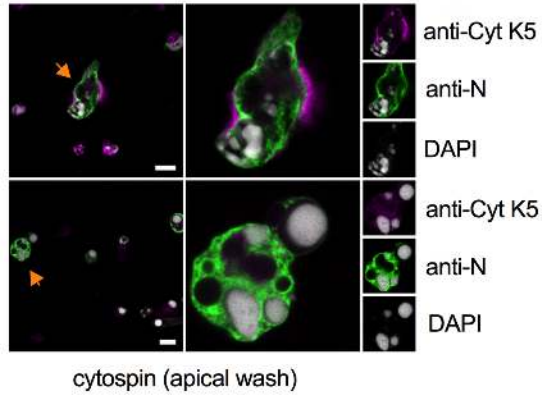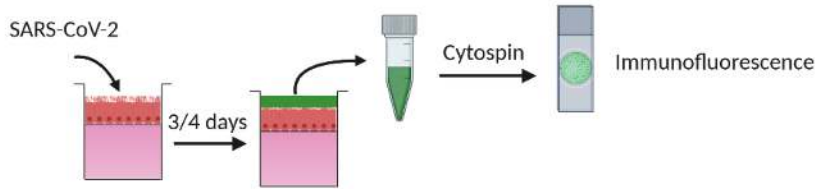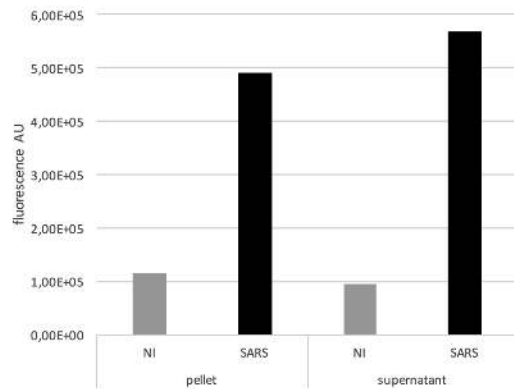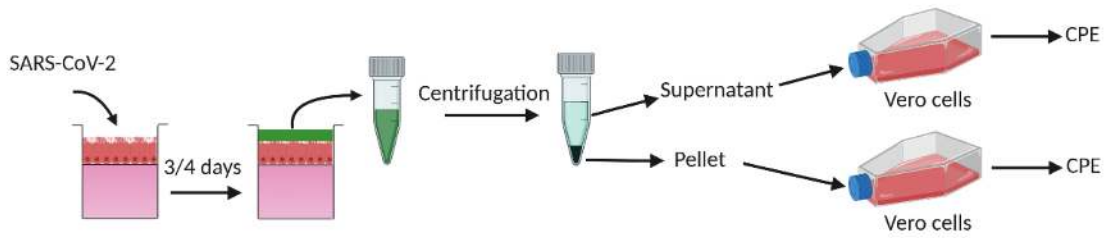
795 **Figure 4.** The apical bronchial epithelia lumen contains infected cells that transmit infection. A: A
796 schematic of the experimental design (top panel). Apical washes at 4 days post-infection were fixed
797 and concentrated on slides using cytospin (bottom panel) and stained with anti-N antibodies to
798 detect infected cells (green signal) and anti-cytokeratin 5 marking basal cells (magenta signal) and
799 counterstained with DAPI (grey signal). Arrows indicate syncytia in the overview and are magnified
800 to the left. The boxed inset is magnified and individual syncytia are indicated by the orange arrows.
801 Scale bar is 10µm. B. A schematic of the experimental design (top panel). Apical washes were
802 separated into supernatant and cell pellet and used to infect Vero E6 cells. CPE was quantified at
803 96h post-infection using fluorescence readout as described in material and methods (Bottom
804 panel).
805
806 <insert page break here>
807

808
809
810

32
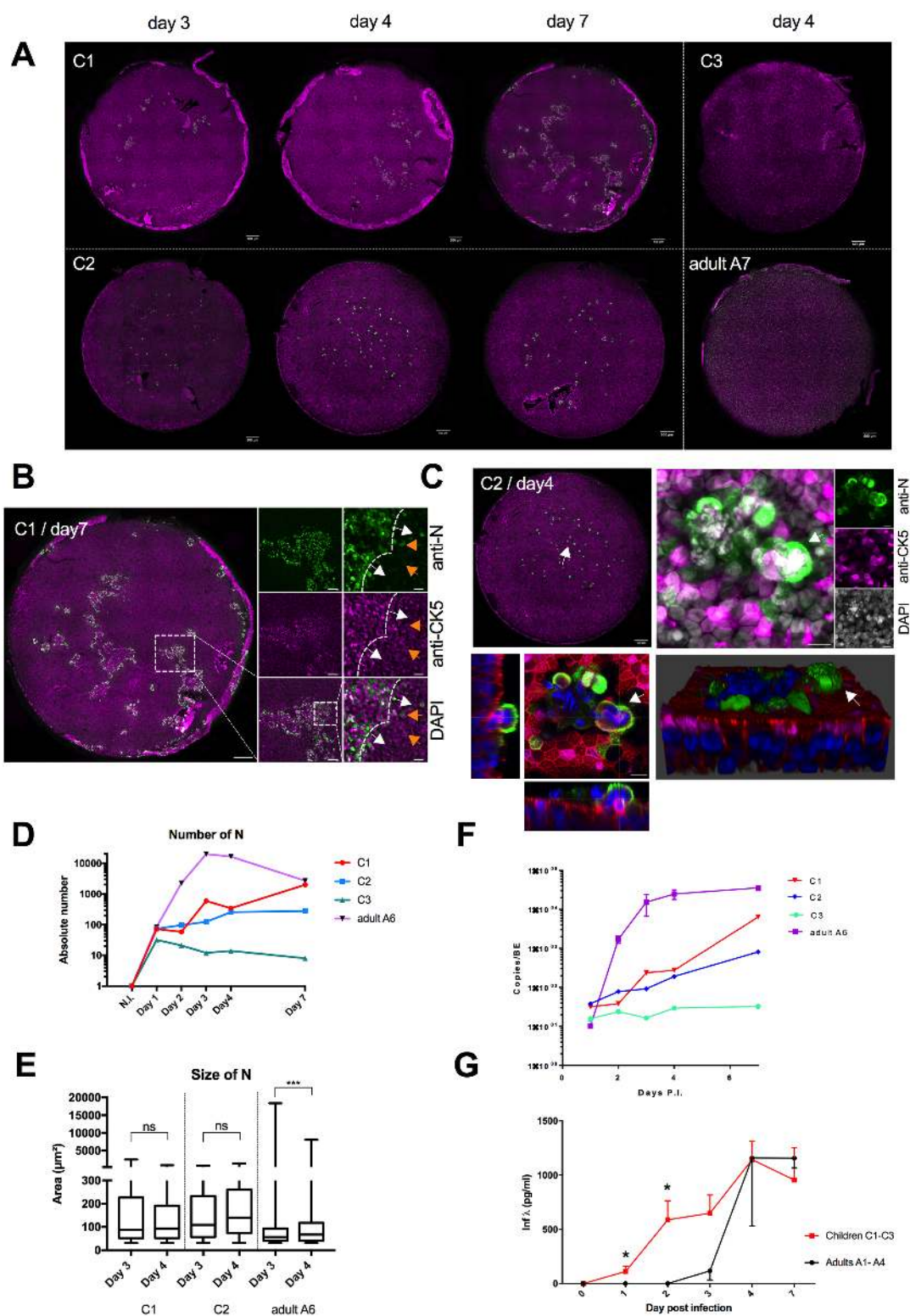
811 **Figure 5.** SARS-CoV-2 infection of bronchial epithelia (BE) in children. A: Overview of entire BE
812 from children and adult control. Donor are as listed in table 1 (C = child, A = adult control) and days
813 post-infection is indicated on the top. BE were stained with anti-N antibodies to detect infected cells
814 (green signal) and anti-cytokeratin 5 marking basal cells (magenta signal). B: High resolution
815 imaging of the Child C1 epithelia 7 days post-infection. Epithelia were stained with anti-N antibodies
816 to detect infected cells (green signal) and anti-cytokeratin 5 marking basal cells (magenta signal).
817 The boxed area containing an infection foci is magnified to the right. The higher magnification
818 shows the infection front (dashed line and white arrows) and individual infected cells in the vicinity
819 of the infection front (orange arrows). C: High resolution imaging of the Child C2 epithelia 4 days
820 post-infection. Epithelia were stained with anti-N antibodies to detect infected cells (green signal)
821 and anti-cytokeratin 5 marking basal cells (magenta signal) and counterstained with DAPi (grey or
822 blue signal). The white arrow in the overview points at a syncytium that is further magnified as
823 maximum Z-projection (left panel) or individual Z-stack (right panel with phalloidin counterstain in
824 red), or as 3D image reconstruction to see its apical location. Scale bar is 10µm, 50µm, 200µm
825 respectively. See also movie S9. D: The absolute number of N-positive cells throughout the BE
826 was estimated for three children donor (C1-3) and one adult control (A6). Color code as indicated.
827 E: The average size of N-positive signals from (D) was determined for two child epithelia (C1 and
828 C2) and one adult control (A6) at 3 and 4 days post-infection as indicated. F: Apical washes for
829 each BE were subject to RT-qPCR analysis to determine genome copy numbers at day 1, 2, 3, 4,
830 and 7 post-infection as indicated. Color code same as in (D). G: Basolateral supernatant from adults
831 (black, n=4) and children (red, n=3) BE were subject to ELISA to determine interferon λ
832 concentration at day 0, 1, 2, 3, 4 and 7 post-infection as indicated. Results are presented as mean
833 ± SEM and * indicates significant difference between adults and children for a time point using
834 Mann Whitney t test.
835
836
837
838
839 <insert page break here>

840

841
842
843   **Table 1.**

Patients	Sexe	Age	BMI
Adult A1	F	46	23
Adult A2	M	58	25
Adult A3	F	54	24
Adult A4	M	63	25
Adult A5	M	51	25
Adult A6	F	61	21
Child C1	F	13	17
Child C2	M	12	16
Child C3	F	12	18

844
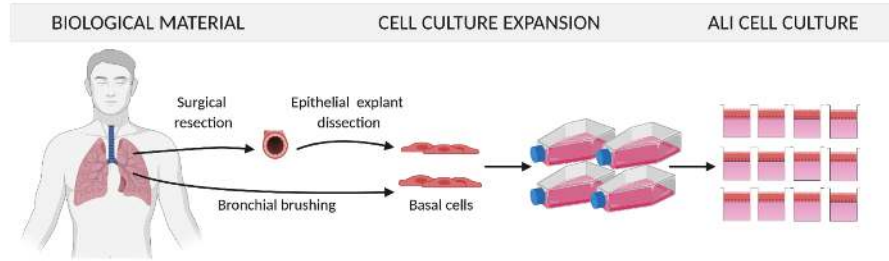845   **Table 1:** Clinical characteristics of adults and children donors used in this study. F: Female: M:
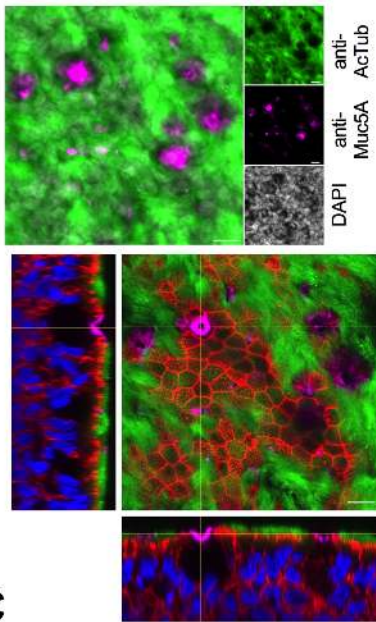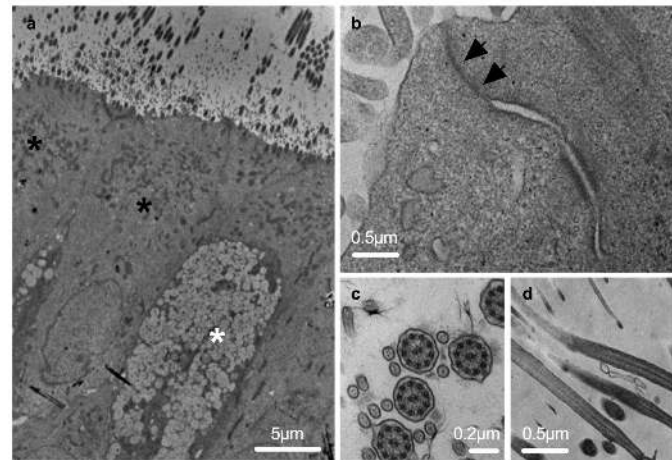846   Male; BMI: Body Mass Index.
847
848   <insert page break here>
849
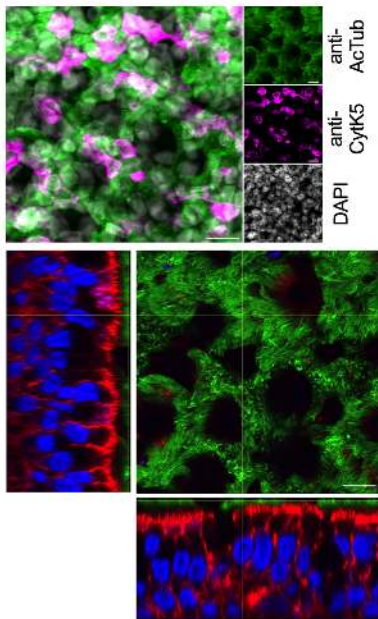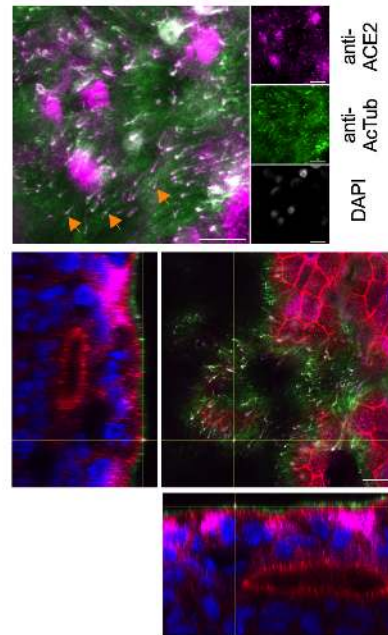
851   **Figure S1.** Characterization of bronchial epithelia (BE). A: Schematic overview of BE generation.
852   Basal cells extracted from surgical dissection or bronchial brushing were expanded and
853   differentiated at the air-liquid interface. B: Differentiated BE were stained with anti-acetylated
854   tubulin to identify ciliated epithelia cells (green signal) or anti-Muc5A to detect cells (pink signal)
855   and counterstained with DAPI (grey in top image, blue in bottom image). Top image shows a Z-
856   projection, the bottom image shows an individual Z-section of a 3D reconstruction counterstained
857   with phalloidin to detect the cell morphology via the actin cell cortex (red signal). Scale bar is 10µm.
858   Note that ciliated cells are located to the apical side (see movie S1 for 3D). C: As in B but the
859   differentiated BE was stained with with anti-acetylated tubulin (green signal) or anti-cytokeratin 5
860   to detect basal cells (pink signal) and counterstained with DAPI. Scale bar is 10µm. (see movie S2
861   for 3D). D: Electron microscopy of fully differentiated BE. The overview (a) shows ciliated epithelia
862   cells (black asterisk) and goblet cells (white asterisk). The magnified images show tight junctions
863   (b) marked by arrows and cilia either as cross-section (c) or longitudinal section (d). Scale bars are
864   indicated. E: As in B but the differentiated BE was stained with with anti-acetylated tubulin (green
865   signal) or anti-ACE2 to detect the SARS-CoV-2 receptor (pink signal) and counterstained with
866   DAPI. Note that arrows point at individual cilia with ACE2 signal. Scale bar is 10µm. (see movie S2
867   for 3D).
868
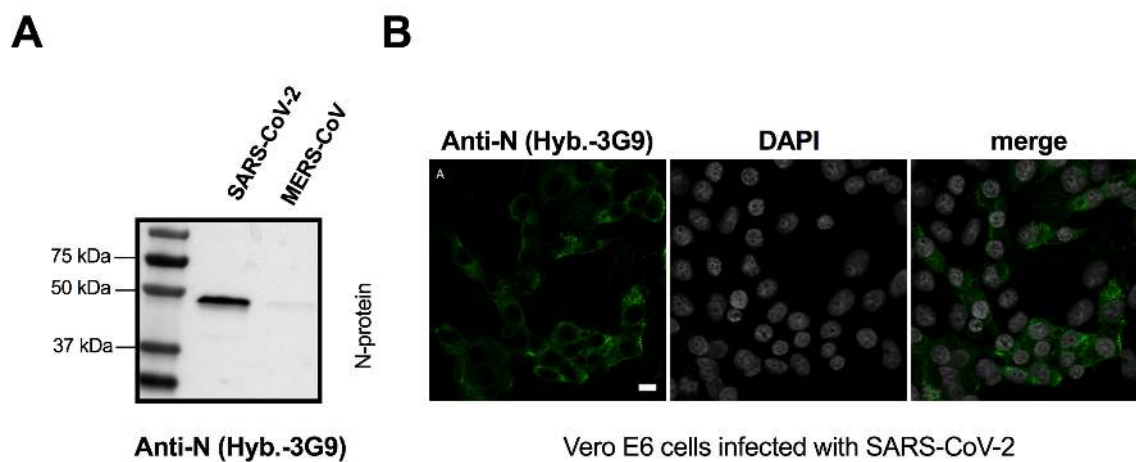
873 **Figure S2.** Characterization of monoclonal anti-SARS-CoV-2-N antibody (clone 3G9). A: Western
874 blot analysis of recombinant bacterially purified SARS-CoV-2-N (100 ng, left lane) vs. MERS-CoV-
875 N (100 ng, right lane). B: Detection of infected Vero E6 cells. Cells were infected for 24h with SARS-
876 CoV-2, fixed and stained with monoclonal antibody to the nucleoprotein of SARS-CoV-2
877 (hybridoma 3G9).
878

879
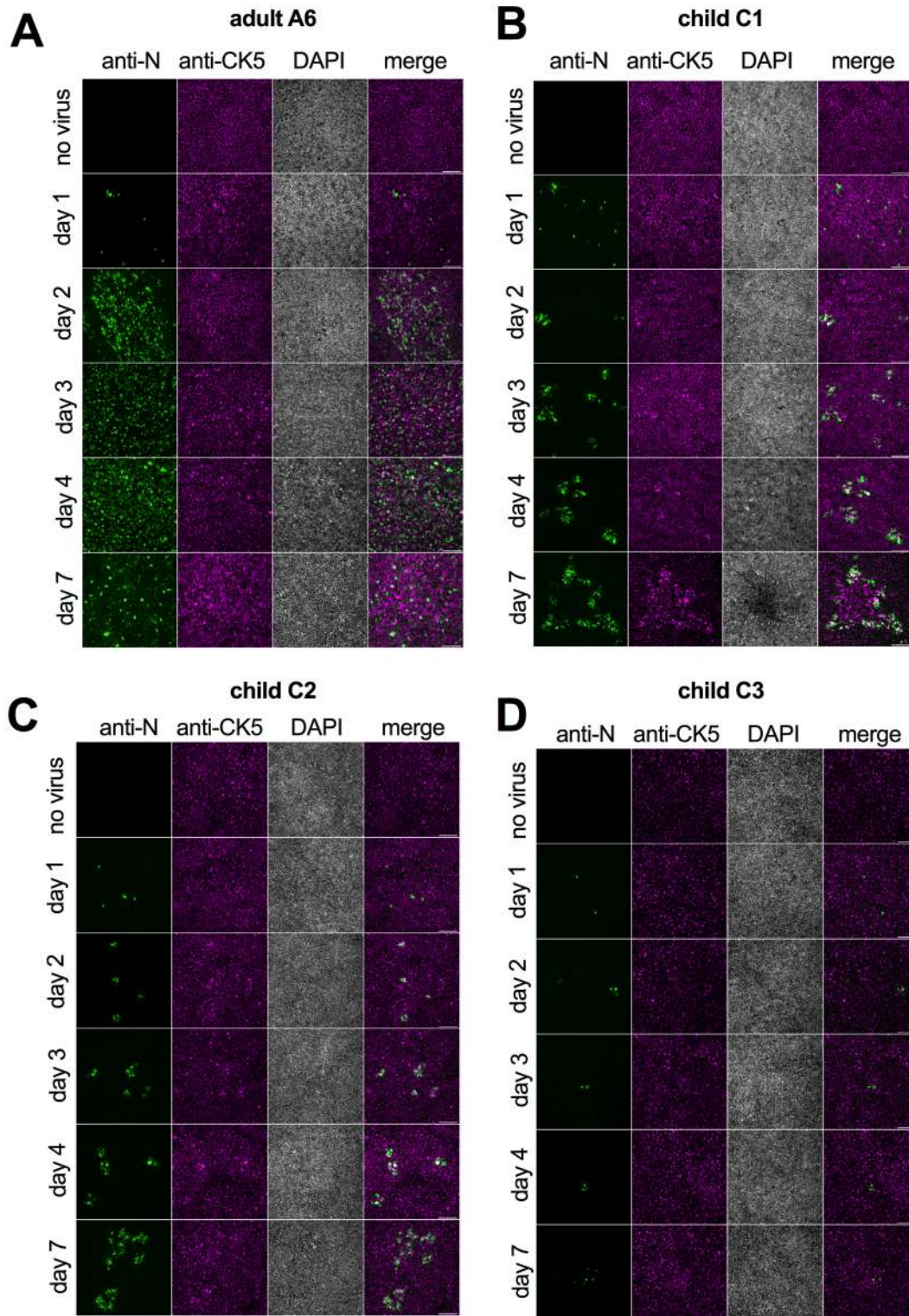
880

881

882 **Figure S3.** SARS-CoV-2 infection kinetic of bronchial epithelia (BE) from children and adult donor.
883 A: Representative widefield microscopy images of BE from one adult donor and three children (A6
884 top left, C1 top right, C2 bottom left and C3 bottom right) at low resolution. BE were fixed at day 1,
885 2, 3, 4, 7 as indicated to the left of each row, non-infected controls were also fixed at day 7. BE
886 were stained with anti-N antibodies to detect infected cells (green signal first column), anti-
887 cytokeratin 5 to detect basal cells (magenta signal, second column) and counterstained with DAPI
888 (grey signal, third column) and a merge of the three signals (forth column). Note the slow virus
889 spread in the children derived epithelia. Scale bar is 10µm

890